NASA Contractor Report 4556

Active Control of Wake/Blade-Row Interaction Noise Through the Use of Blade Surface Actuators

Kenneth A. Kousen and Joseph M. Verdon
United Technologies Research Center
East Hartford, Connecticut

NASA

National Aeronautics and
Space Administration

Office of Management

Scientific and Technical
Information Program

1993

Active Control of Wake/Blade-Row Interaction Noise Through the Use Of Blade Surface Actuators

Contents

Active Control of Wake/Blade-Row Interaction Noise Through the Use of Blade Surface Actuators

Kenneth A. Kousen and Joseph M. Verdon
United Technologies Research Center
East Hartford, Connecticut 06108-1049

Summary

This report describes a combined analytical/computational approach for controlling of the noise generated by wake/blade-row interaction through the use of anti-sound actuators on the blade surfaces. A representative two-dimensional section of a fan stage, composed of an upstream fan rotor and a downstream fan exit guide vane (FEGV), is examined. An existing model for the wakes generated by the rotor is analyzed to provide realistic magnitudes for the vortical excitations imposed at the inlet to the FEGV. The acoustic response of the FEGV is determined at multiples of the blade passing frequency (BPF) by using the linearized unsteady flow analysis, LINFLO. Acoustic field contours are presented at each multiple of BPF illustrating the generated acoustic response disturbances. Anti-sound is then provided by placing oscillating control surfaces, whose lengths and locations are specified arbitrarily, on the blades. An analysis is then conducted to determine the complex amplitudes required for the control surface motions to best reduce the noise. It is demonstrated that if the number of acoustic response modes to be controlled is equal to the number of available independent control surfaces, complete noise cancellation can be achieved. A weighted least squares minimization procedure for the control equations is given for cases in which the number of acoustic modes exceeds the number of available control surfaces. The effectiveness of the control is measured by the magnitude of a propagating acoustic response vector, which is related to the circumferentially averaged sound pressure level (SPL), and is minimized by a standard least-squares minimization procedure.

1

1. Introduction

Aerodynamically-induced engine noise is becoming an increasingly important subject. The noise produced by an engine arises from a variety of sources, but of particular concern are the discrete frequency tones generated through fan rotor/stator interaction. These tones are quite annoying to a listener, and represent a significant environmental concern [1]. The discrete tones appear in an engine noise spectrum as spikes at multiples of the blade passing frequency (BPF), whose magnitudes are significantly higher than the background broadband noise levels. It has been observed that noise reduction methods aimed at lowering broadband noise can make the perceived noise problem worse, by further emphasizing the discrete tones. Consequently, the turbomachinery designer is faced with the responsibility of reducing discrete tone noise directly.

A major source of engine discrete tone noise is that generated within a fan stage by the interaction of the wakes from the fan rotor with the blades of the fan exit guide vane (FEGV). This interaction creates acoustic response waves, which under certain conditions propagate unattenuated in amplitude as they move upstream and downstream from the FEGV. The propagating acoustic response modes therefore provide targets for control analyses aimed at reducing discrete tone noise.

In this report, we examine the noise generated by wake/blade-row interaction in a fan stage, and investigate one possible strategy, namely the generation of anti-sound by the oscillations of blade surface actuators, for reducing this noise. Control is provided by adjusting the amplitudes of the control surface, or piston, motions on the FEGV blades, to produce acoustic response modes that are 180 degrees out of phase with the undesired response. The superposition of the acoustic responses due to external excitations, i.e., those associated with the rotor wakes, with those due to the control surface motions, results in a reduced net acoustic response.

Active control of noise is an active area of research [2, 3, 4, 5, 6, 7], but applications to the turbofan engine noise problem have only recently begun to appear [8, 9]. The experimental studies in [8] and [9] suggest that the introduction of antisound as a means of active control of turbomachinery noise may be a promising approach. The present report provides a computational simulation of turbomachinery noise under realistic operating conditions, and its subsequent control.

Section 2.1 of this report presents the analyses used to determine the vortical and entropic excitations that represent the rotor wakes as seen by the stator. The linearized unsteady analyis, LINFLO [10, 11], which is reviewed in Section 2.2, provides a means for determining the acoustic response of the FEGV to the vortical and entropic excitations. Since the acoustic response of the FEGV is primarily attributable to vortical excitations, the entropic excitations are not employed in the subsequent control analysis. Section 3 contains control algorithms developed to reduce the undesired acoustic responses. It is observed that if the number of independent control surface actuators is equal to the number of propagating acoustic response modes, then oscillation amplitudes of the actuators can be found that result in a complete elimination of the noise. Analyses are also provided, based on weighted least-squares minimization procedures, for reducing the noise as much as possible in the more general case, where the number of propagating response modes exceeds the number of

2

control surfaces. Results of the active control analyses, both for complete cancellation and least squares minimization, are shown in Section 4. These analyses are intended to provide a demonstration of the potential of active noise control through the use of blade surface actuators, as a method for reducing discrete tone turbomachinery noise.

2. Physical Problem

A two-dimensional representation of a typical fan stage is shown in Fig. 2.1. In each row, upstream flow quantities are indicated by a subscript $-\infty$, while downstream quantites are shown by a subscript $+\infty$. The wheel velocity of the fan rotor cascade is $\mathbf{V}_W$. Total ($\tilde{\mathbf{V}}$) and mean ($\mathbf{V}$) velocity components are given in the figure with and without tildes, respectively. Where confusion between reference frames might occur, primes are used to denote quantities associated with the fan rotor.

Axial and circumferential distances are represented via the Cartesian coordinate systems (ξ', η') and (ξ, η) rigidly attached to the fan and FEGV rows, respectively. For the FEGV row, the mean or steady-state positions of the blade chord lines coincide with the line segments $\eta = \xi \tan \Theta + mG, 0 \leq \xi \leq \cos \Theta, m = 0, \pm 1, \pm 2, \ldots$, where m is a blade number index, Θ is the cascade stagger angle, and $\mathbf{G}$ is the gap vector which is directed along the η-axis with magnitude equal to the blade spacing. Fan cascade quantities are defined analogously.

The velocity triangle relationships representing the transformation of velocities from rotor-fixed to stator-fixed coordinates are examined in the general discussion of the wake analysis below, which determines the vortical and entropic excitations resulting from the fan wakes. Subsequently, the linearized unsteady flow analysis LINFLO is reviewed, which shows how the vortical excitations are used in a numerical calculation of the resultant acoustic response of the FEGV.

2.1   Wake Excitation Model

The LINFLO analysis determines the acoustic response of a blade row to individual Fourier modes of a vortical or entropic disturbance imposed at the inlet to the blade row. The goal of the wake analysis, therefore, is to determine these Fourier modes through an analysis of the fan wakes and a transformation from rotor-fixed to stator-fixed coordinates. The flow within each wake is assumed to be parallel and aligned with the mean exit flow direction of the rotor, and is characterized by a given velocity profile, centerline velocity defect $V'_{\min}/V'_e$, and wake half-width δ, which are defined below. The wakes have a circumferential period equal to the rotor gap G'. In addition, it is assumed that across each wake, the static pressure $\tilde{P}'$ and the total enthalpy $\tilde{H}'_T$ are constant. The assumption of constant static pressure across the fan exit implies that the fan wakes will give rise to velocity disturbances that are purely rotational or vortical in nature. Since the orthogonal components of the velocity disturbances associated with vorticity are not independent, it is sufficient to find the individual Fourier components of $\tilde{\mathbf{v}} \cdot \mathbf{e}_N$, i.e., the component of the disturbance velocity normal to the inlet flow direction of the FEGV, at each multiple of BPF. These quantities will be found in terms of the wake shape parameters, the stator inlet flow properties, the rotor wheel speed, and the gap to chord ratios for each row. Finally, the assumption of constant total enthalpy provides a link between the disturbance velocity components arising from the wakes, and the associated disturbance entropy components.

The velocity triangle for the region between the rotor and stator is shown in Fig. 2.1. Both the total velocity and the mean velocity from the rotor row, designated $\tilde{\mathbf{V}}'_{+\infty}$ and $\mathbf{V}'_{+\infty}$ respectively, are seen to be oriented at the exit flow angle $\Omega'_{+\infty}$ of the rotor. The rotor moves
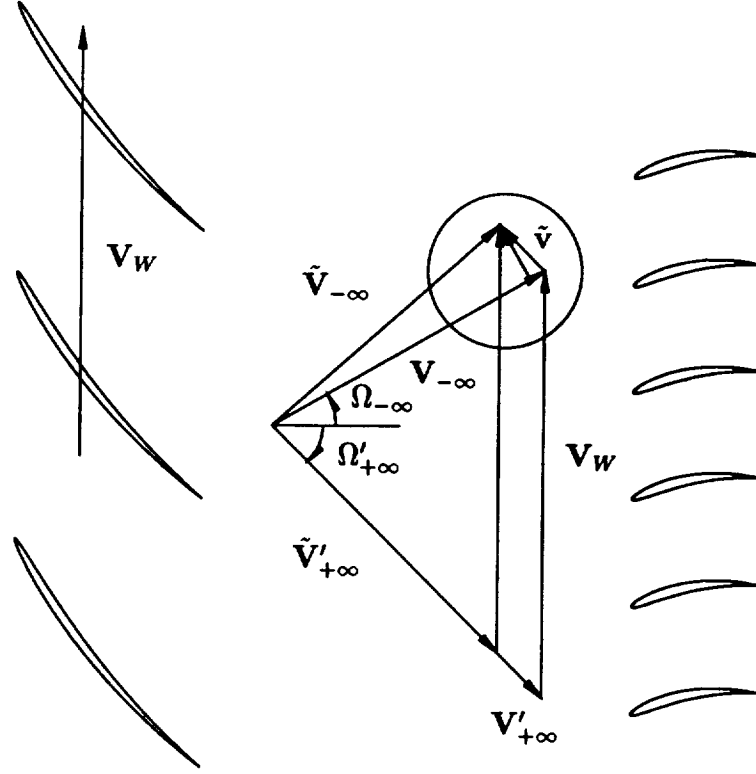
4

Figure 2.1: Velocity triangles for fan rotor/fan exit guide vane configuration.

at a wheel speed of V_W in the positive η' direction. By adding the wheel velocity vectorially to the mean and total exit flow velocities of the rotor, the mean and total inlet flow velocities, $\mathbf{V}_{-\infty}$ and $\tilde{\mathbf{V}}_{-\infty}$, respectively, to the stator can be found. The difference between the mean and total inlet velocities to the stator defines the perturbation velocity $\tilde{\mathbf{v}}$, i.e.,

$$\tilde{\mathbf{v}} = \tilde{\mathbf{V}}'_{+\infty} - \mathbf{V}'_{+\infty}. \tag{2.1}$$

Consequently, the perturbation velocity can be found by an analysis of excitation row quantities alone.

In keeping with the notation of Ref. [12], the symbols v^+ and u^+ will be used to represent the components of $\tilde{\mathbf{v}}$ in directions normal and tangential to the inlet mean flow velocity of the stator (Fig. 2.2). From the figure, the component v^+ is found to be

$$v^+ = \tilde{\mathbf{v}} \cdot \mathbf{e}_N = (V'_{+\infty} - \tilde{V}'_{+\infty}) \sin(\Omega'_{+\infty} - \Omega_{-\infty}), \tag{2.2}$$

where $\mathbf{e}_N$ is a unit vector normal to the stator inlet flow direction.

In the rotor frame of reference, the wake velocity can be expressed as a Fourier series in the circumferential direction, whose zeroth component can be identified as the mean velocity. Consequently, v^+ can also be expressed as a Fourier series, whose individual components are given by

$$v^+(\eta') = \sum_{n=-\infty}^{\infty} v_n^+ \exp(in\kappa_n\eta'), \tag{2.3}$$
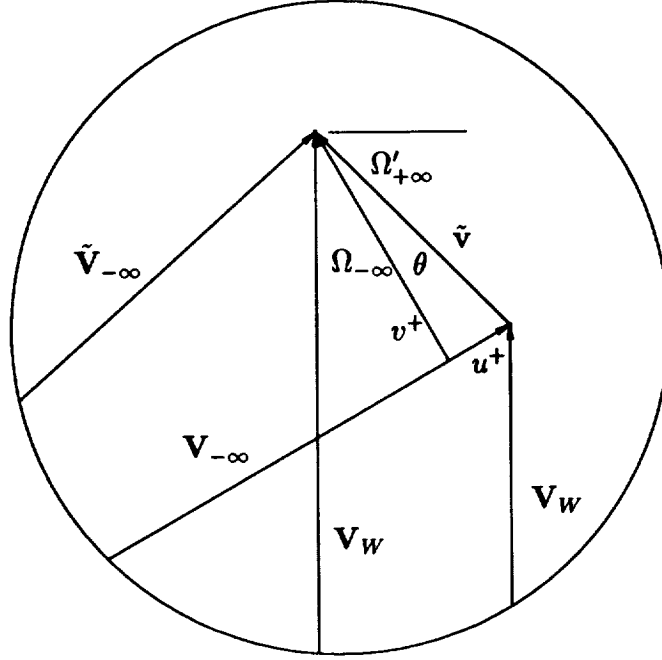
5

Figure 2.2: Magnification of the circled region from the velocity triangle.

where $\kappa_\eta = 2\pi/G'$ is the circumferential wavenumber of the vortical excitation, G' is the gap to chord ratio for the rotor, and

$$v_n^+ = \frac{1}{G'} \int_{\eta'_{\text{ref}}}^{\eta'_{\text{ref}}+G'} \tilde{\mathbf{v}} \cdot \mathbf{e}_N \exp(-in\kappa_\eta\eta') \, d\eta' , \qquad (2.4)$$

where η'_{ref} is a reference location in the rotor frame.

Note that the rotor-fixed and stator-fixed coordinates are related by $\mathbf{x}' = \mathbf{x} - \mathbf{V}_W t$, where $\mathbf{x}' = (\xi', \eta')$ is a position vector in the moving frame attached to the rotor, and $\mathbf{x} = (\xi, \eta)$ is a position vector in the stationary reference frame. Therefore, the v_n^+ components defined by Eq.(2.3) in the rotor frame can be expressed as

$$v^+ = \sum_{n=-\infty}^{\infty} v_n^+ \exp(in\kappa_\eta\eta) \exp(-in\kappa_\eta V_W t) \qquad (2.5)$$

in the stator frame, which demonstrates that while the disturbance velocity is steady in the rotating frame, it provides a set of unsteady disturbances in the stationary frame with frequencies $\omega_n = -n\kappa_\eta V_W$. The interblade phase angles σ_n of these disturbances are found from the circumferential wavenumber and the gap to chord ratio of the stator row, i.e.,
$\sigma_n = n\kappa_\eta G$.

Wake parameters

To evaluate the v_n^+ components, it is thus necessary to have an expression for the rotor exit velocity, $\tilde{\mathbf{V}}'_{+\infty}$. This velocity will be evaluated by using the semi-empirical rotor wake

6

model of Majjigi and Gliebe [13], which defines the wake velocity at streamwise locations downstream of the rotor in terms of a shape function, a centerline velocity defect, and a wake half-width. The behavior of these quantities will be described below, as will their implementation into the analysis for the calculation of the vortical and entropic excitations to the FEGV.

The rotor wakes are assumed to be aligned with the exit flow direction of the rotor, and to be identical from blade to blade. In terms of a Cartesian coordinate system (T', N') tangential and normal to the rotor exit flow angle, with origin at the rotor blade trailing edge, the velocity in a reference wake can be expressed as

$$V'(T', N')\, \mathbf{e}_{T'} = V'_e(T') \left(1 - \frac{V'_{\text{def}}}{V'_{\text{min}}} \frac{V'_{\text{min}}}{V'_e}\right) \mathbf{e}_{T'}, \qquad (2.6)$$

where $V'_e(T')$ is the velocity at the edge of a wake, $V'_{\text{def}}(N')$ is the wake deficit, defined as the difference between the edge velocity and the velocity in the wake, at each N', V'_{min} is the minimum streamwise velocity across the wake, and $\mathbf{e}_{T'}$ is a unit vector tangential to the rotor exit flow direction. The quantity $V'_{\text{def}}/V'_{\text{min}} = f(N')$ is a shape function that is dependent only on the normal coordinate, N'. The wakes are assumed here to be symmetric, so the minimum velocity occurs at the wake centerline and the quantity V'_{min}/V'_e will be hereafter referred to as the centerline velocity defect. Two different shape functions are usually considered, a hyperbolic secant function or a Gaussian function. A given wake velocity distribution is made unique by specifying the shape function, the centerline velocity defect, and the wake half-width, which is defined as the distance between the points where the wake deficit is half its maximum value. The shape functions are therefore given by

$$f(N') = \text{sech}\left[\frac{2}{\delta}(\cosh^{-1}2)N'\right] \qquad (2.7)$$

for the hyperbolic secant profile, or

$$f(N') = \exp\left[-\frac{4}{\delta^2}(\ln 2)N'^2\right] \qquad (2.8)$$

for the Gaussian profile. The hyperbolic secant profile is used in the results presented below. The centerline defect V'_{min}/V'_e and the half-width δ are given by the empirically determined functions [13]

$$\frac{V'_{\text{min}}}{V'_e} = C_D^{1/4}\left(\frac{0.3675\, T' + 1.95}{7.65\, T' + 1.0}\right) \qquad (2.9)$$

and

$$\delta = \frac{0.2375 C_D^{1/8}\, T' + 0.034125}{0.357 C_D^{1/8}\, T' + 1.0}, \qquad (2.10)$$

where C_D is the section drag coefficient. In these equations, the streamwise distance T' and the wake half-width δ have been nondimensionalized by the rotor chord. A typical wake velocity profile, based on the hyperbolic secant shape function, is shown in Fig. 2.3. Fig. 2.4 shows the variation of the centerline velocity defect and the half-width with increasing streamwise distance from the fan rotor under consideration. Note that the decay of the
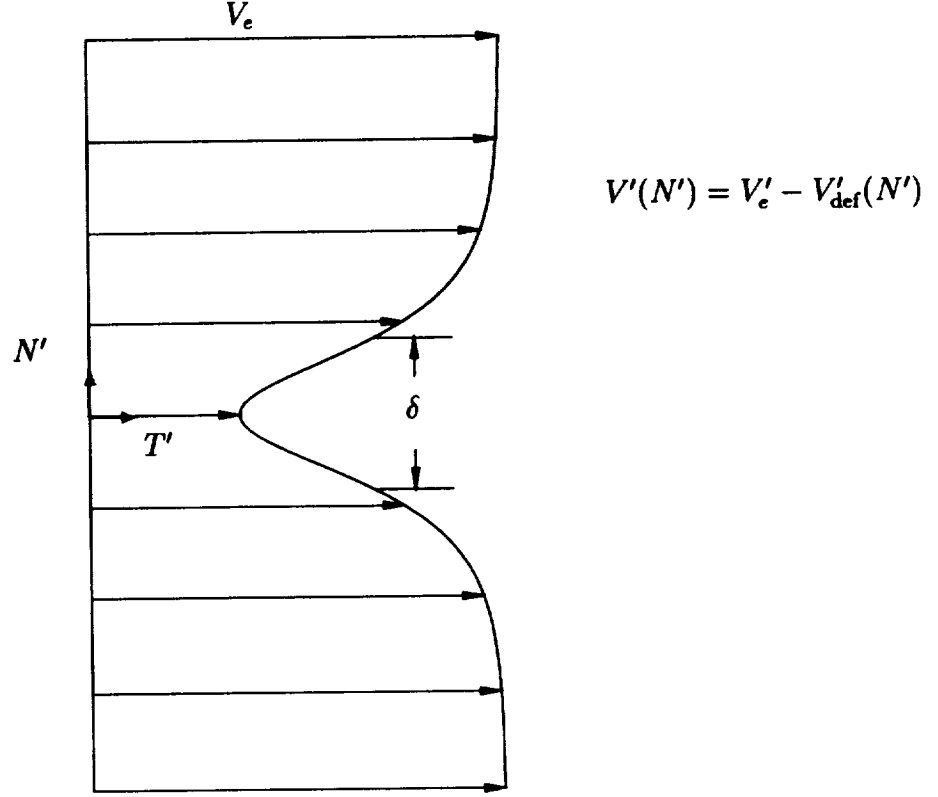
7

$$V'(N') = V_e' - V'_{\text{def}}(N')$$

Figure 2.3: Typical wake profile $V'(N) = V_e' - V'_{\text{def}}(N')$, where V_e' is the edge velocity, δ is the wake half-width, and $V'_{\text{def}}(N')$ is the velocity deficit at each N'.

centerline velocity defect occurs primarily in the near wake.

After determining the velocity distribution across the wake, the Fourier decomposition in Eq. (2.4) must be performed on the component of this velocity normal to the inlet flow direction for the stator, at an appropriate axial ξ' location downstream of the rotor. The results of the Fourier decomposition then yield the v_n^+ values in Eq. (2.3). Note that care must be taken to ensure that all velocities are nondimensionalized with respect to the mean inlet flow velocity to the stator. In terms of a given centerline velocity defect, the rotor wake edge velocity can be shown to be

$$V_e' = \frac{V'_{+\infty}}{1 - \dfrac{1}{G'}\dfrac{V'_{\min}}{V_e'}\displaystyle\int_{\eta'_{\text{ref}}}^{\eta'_{\text{ref}}+G'} f(\eta')d\eta'}, \qquad (2.11)$$

where the mean exit flow velocity of the rotor can be expressed in terms of the stator row inlet flow angle and the wheel speed by

$$V'_{+\infty} = \sqrt{1 + V_W^2 - 2V_W \sin\Omega_{-\infty}}. \qquad (2.12)$$

Values for the v_n^+'s have been determined at several axial stations within the region between the fan rotor and FEGV. The wake profiles were determined by evaluating the
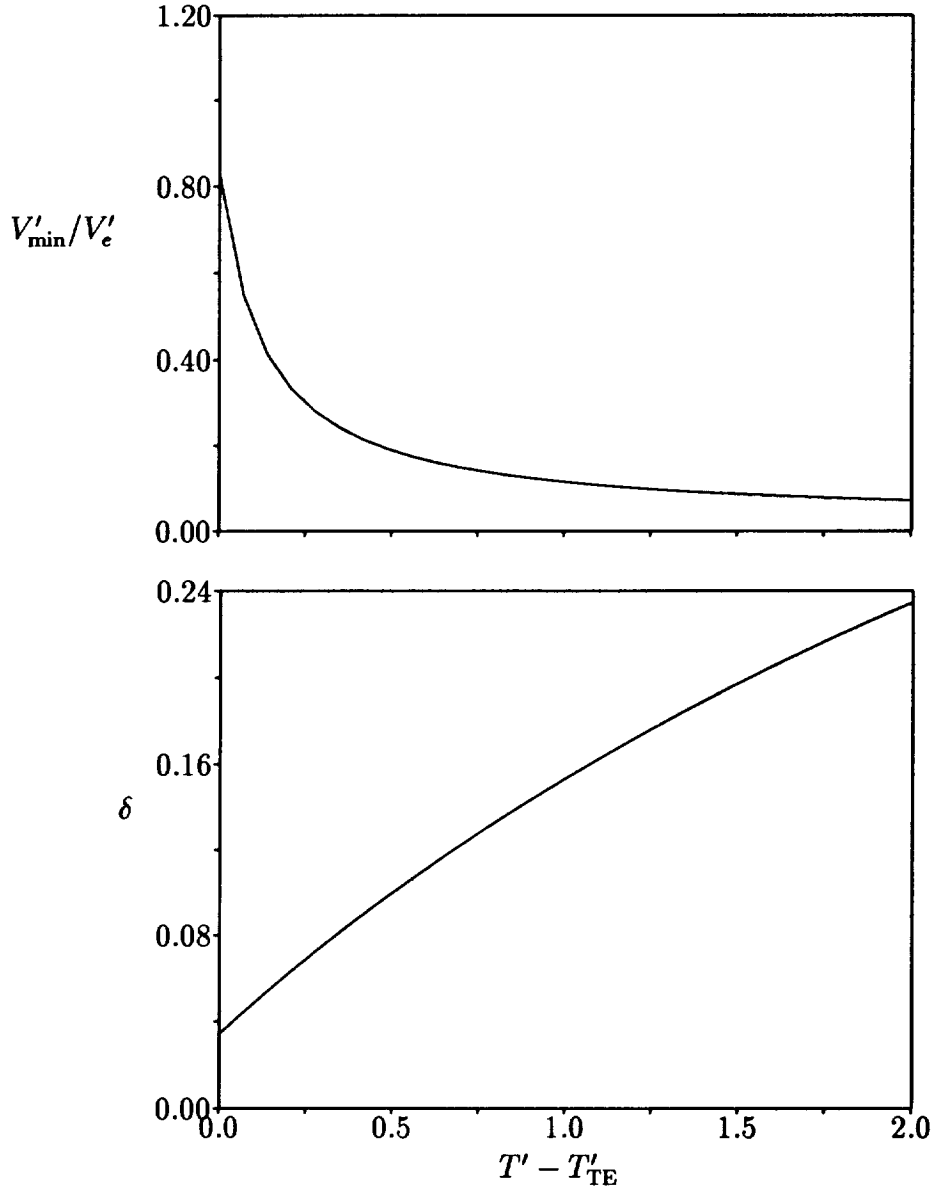
8

Figure 2.4: Variation in centerline velocity defect, V'_{min}/V'_e, and wake half-width, δ, with stream-wise distance along a blade wake for a representative fan rotor.

parameters δ and V'_{min}/V'_e at each axial station through the empirical relations in Eqs. (2.9) and (2.10), after a transformation from (ξ', η') to (T', N') coordinates. Typical results for the variation in the magnitudes $|v_n^+|$, $n = 1, 2, \ldots, 6$, of the complex amplitudes v_n^+ with increasing axial distance are shown in Fig. 2.5. Note that there is an initial decay in the magnitude of each component followed by a much more gradual decrease with axial distance. Also, the decay is more pronounced for the higher order components.

The inviscid analysis of the FEGV imposes the vortical exitations at the inlet of the FEGV row. Since vortical and entropic disturbances are convected through the response row, their magnitudes are unaltered. Figure 2.5 demonstrates that if the axial spacing
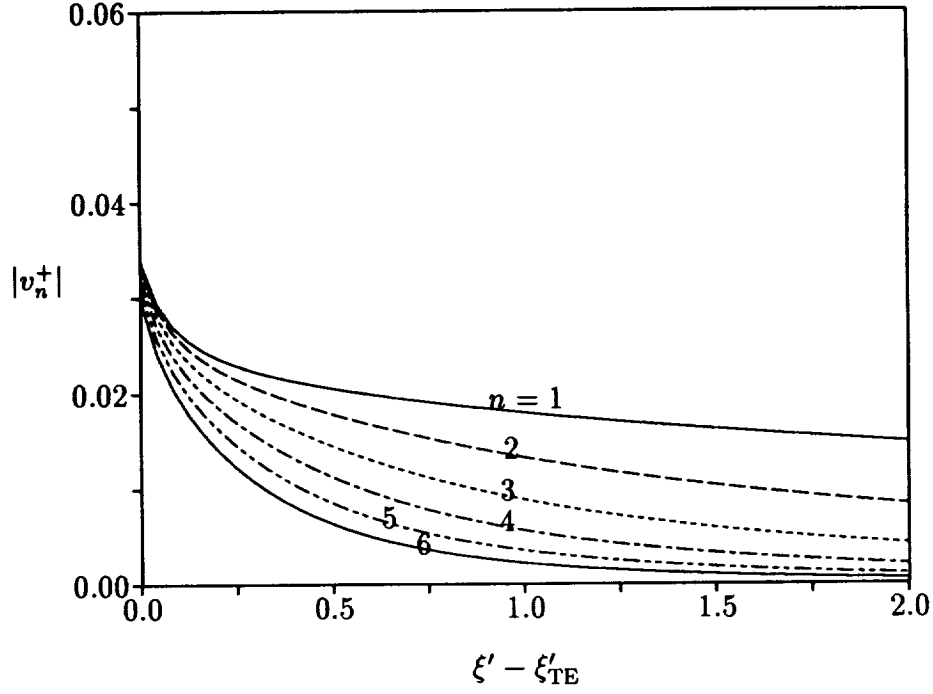
Figure 2.5: Variation of the magnitudes of the complex Fourier components $|v_n^+|$ with axial distance downstream of the trailing edge of the fan rotor.

between the blade rows is sufficiently large, the magnitudes of the Fourier components will not vary substantially. It is necessary, however, to choose an axial location at which the v_n^+ components will be evaluated. Common practice suggests that the leading edge of the response blades is a reasonable choice, and will be adopted herein.

Entropic disturbances

It has been assumed that the fluid pressure and total enthalpy are constant across each wake. These restrictions can be used to relate the entropic disturbances associated with the wakes to the velocity disturbances associated with the wake vorticity. The total enthalpy downstream of the fan rotor is given by

$$\tilde{H}'_{T,+\infty} = \tilde{H}'_{+\infty} + \frac{1}{2}\tilde{\mathbf{V}}'_{+\infty} \cdot \tilde{\mathbf{V}}'_{+\infty} = \gamma(\gamma-1)^{-1}\tilde{P}'_{+\infty}/\tilde{\rho}'_{+\infty} + \frac{1}{2}\tilde{\mathbf{V}}'_{+\infty} \cdot \tilde{\mathbf{V}}'_{+\infty}, \qquad (2.13)$$

where $\tilde{H}'_{+\infty}$ is the static enthalpy. After linearizing this relation, setting $\tilde{H}'_{T,+\infty} = H'_{T,+\infty}$, $\tilde{P}'_{+\infty} = P'_{+\infty}$, and introducing the thermodynamic relation $s'_{+\infty} = \gamma^{-1}\tilde{p}'_{+\infty}/P'_{+\infty} - \tilde{\rho}'_{+\infty}/\bar{\rho}'_{+\infty}$, we find that

$$\tilde{s}'_{+\infty} = -\gamma^{-1}(\gamma-1)\bar{\rho}'_{+\infty}\mathbf{V}'_{+\infty} \cdot \tilde{\mathbf{v}}'_{+\infty}/P'_{+\infty} = -(\gamma-1)\mathbf{V}'_{+\infty} \cdot \tilde{\mathbf{v}}'_{+\infty}/(A'_{+\infty})^2 \qquad (2.14)$$

where $A^2 = \gamma P/\bar{\rho}$ is the speed of sound propagation in the mean flow. From Fig. 2.1, it can be seen that $\mathbf{V}'_{+\infty} \cdot \tilde{\mathbf{v}}'_{+\infty} = V'_{+\infty}\tilde{v}'_{+\infty}$. In addition, $s'_{+\infty} = s_{-\infty}$ and $v'_{+\infty} = v_{-\infty}$. Therefore,

10

the disturbance entropy that acts as the excitation at the inlet of the FEGV is given by

$$\tilde{s}_{-\infty} = (1 - \gamma)M'_{+\infty}\tilde{v}_{-\infty}/A'_{+\infty} \tag{2.15}$$

where $\tilde{v}_{-\infty}$ is the complex amplitude of the velocity disturbance associated with the vortical excitation. The relative exit Mach number from the rotor can be related to the inlet Mach number of the stator through the relation $M'_{+\infty} = V'_{+\infty}M_{-\infty}$, since the nondimensional inlet mean velocity to the stator has magnitude one. The complex amplitude of the nth component of the disturbance entropy is given by

$$s_{-\infty,n} = (1 - \gamma)M'_{+\infty}M_{-\infty}v_{-\infty,n} \tag{2.16}$$

where the Mach numbers $M'_{+\infty}$ and $M_{-\infty}$ are based on the relative flow speeds, $V'_{+\infty}$ and $V_{-\infty}$, respectively.

In summary, the wake flows are assumed to be parallel, aligned along the rotor exit flow angle, with constant total enthalpy and constant static pressure. At an axial location corresponding to the leading edge of the stator row, the wake velocity distribution is calculated using a shape function (cf. Eq. (2.7) or (2.8)), a centerline velocity defect at that location, which is found from Eq. (2.9), and a wake half-width at that location, which is evaluated from Eq. (2.10). By performing a Fourier decomposition on the component of the wake velocity normal to the inlet flow direction of the stator, v_n^+ values are found via Eq. (2.4). The magnitudes of entropic excitations corresponding to the v_n^+ values can then be determined as well. The inlet vortical and entropic disturbances to the FEGV are characterized by interblade phase angles $\sigma_n = n\sigma = n\kappa_\eta G$, and frequencies $\omega_n = n\omega = -n\kappa_\eta V_W$, and are imposed at the inlet of the stator row, where an inviscid analysis numerically determines the resulting acoustic response.

2.2 Unsteady Flow through the Stator Blade Row

This section summarizes the method for calculating the unsteady pressure response of the FEGV to the imposed vortical and entropic excitations found from the wake analysis. The response is calculated using the LINFLO analysis [10, 11]. The entire analysis in this section will be performed in the stator frame of reference.

The flow through the FEGV is considered to be a time-dependent, adiabatic, attached subsonic flow, with negligible body forces, of an inviscid non-heat-conducting, perfect gas. It is assumed that in the absence of unsteady excitation the mean flow is uniform at the inlet to the FEGV. The unsteady fluctuations in the flow arise from the entropic or vortical excitations at inlet, as well as the motions of control surfaces on the blades. All the excitations are assumed to be of small amplitude, periodic in time, and periodic in the η-direction.

Control surface motions will be modeled as prescribed blade motions of the form

$$\mathcal{R}_B(\mathbf{x} + mG, t) = \text{Re}\{\mathbf{r}_B(\mathbf{x})\exp[i(\omega t + m\sigma)]\} \quad \mathbf{x} \in \text{B} . \tag{2.17}$$

that are restricted to portions of the blade surfaces. Here $\mathcal{R}_B$ measures the displacement of a point on a blade surface relative to its mean or steady-state position, $\mathbf{x}$ is a position vector, t is time, $\mathbf{r}_B$ is a complex displacement-amplitude vector, Re{ } denotes the real part

11

of { } and B denotes the reference ($m = 0$) blade surface. The incident disturbances are prescribed as functions of $\mathbf{x}$ and t which satisfy the field equations that govern the unsteady flow. Thus, small-amplitude entropic and vortical fluctuations relative to a uniform stream must be of the form

$$\tilde{s}_{-\infty}(\mathbf{x}, t) = \text{Re}\{s_{-\infty} \exp[i(\boldsymbol{\kappa}_{-\infty} \cdot \mathbf{x} + \omega t)]\} \dots , \quad \xi < \xi_- , \qquad (2.18)$$

and

$$\tilde{\boldsymbol{\zeta}}_{-\infty}(\mathbf{x}, t) = \text{Re}\{\boldsymbol{\zeta}_{-\infty} \exp[i(\boldsymbol{\kappa}_{-\infty} \cdot \mathbf{x} + \omega t)]\} \dots , \quad \xi < \xi_- . \qquad (2.19)$$

Here $s_{-\infty}$ and $\boldsymbol{\zeta}_{-\infty}$ are the (prescribed) complex amplitudes of the entropic and vortical fluctuations, $\tilde{s}(\mathbf{x}, t)$ and $\tilde{\boldsymbol{\zeta}}(\mathbf{x}, t)$, respectively, far upstream ($\xi < \xi_-$) of the FEGV.

The fluid motion is governed by a coupled set of nonlinear differential equations (i.e., the Euler equations) in continuous regions of the flow, a flow tangency condition at blade surfaces, and jump conditions at vortex-sheet unsteady wakes. In addition, information on the uniform flow conditions at inlet and exit and the entropic and vortical fluctuations at inlet must be specified. Since the unsteady excitations are assumed to be of small-amplitude, the time-dependent flow can be regarded as a small perturbation about an underlying mean or steady flow. This linearization can be performed by substituting relations analogous to that for the time-dependent fluid velocity, i.e.,

$$\tilde{\mathbf{V}}(\mathbf{x}, t) = \mathbf{V}(\mathbf{x}) + \tilde{\mathbf{v}}(\mathbf{x}, t) + \dots , \qquad (2.20)$$

where $\mathbf{V}(\mathbf{x})$ is the local mean velocity, and $\tilde{\mathbf{v}}(\mathbf{x}, t)$ is the first-order (in ϵ) unsteady velocity into the full, time-dependent governing equations and collecting terms of like power in ϵ and neglecting terms of $\mathcal{O}(\epsilon^2)$ or higher. The first-order unsteady fluctuations that arise from the various independent modes of excitation are not coupled and hence, can be determined separately. Indeed, it is sufficient to determine unsteady flow solutions for each single harmonic (in t and η) component of a given disturbance. Solutions for arbitrary disturbances and arbitrary combinations of various disturbances can then be obtained by Fourier superposition.

The first-order or linearized unsteady flow properties caused by a periodic unsteady excitation at temporal frequency ω will be harmonic in time, e.g., $\tilde{\mathbf{v}}(\mathbf{x}, t) = \text{Re}\{\mathbf{v}(\mathbf{x}) \exp(i\omega t)\}$. In addition, the steady and, for an excitation at circumferential wave number $\kappa_\eta = \sigma G^{-1}$, the first-order unsteady properties will satisfy the blade-to-blade periodicity conditions, e.g., $\mathbf{V}(\mathbf{x} + m\mathbf{G}) = \mathbf{V}(\mathbf{x})$ and $\mathbf{v}(\mathbf{x} + m\mathbf{G}) = \mathbf{v}(\mathbf{x}) \exp(im\sigma)$, respectively. Thus, solutions to time-independent nonlinear steady and linearized unsteady flow problems are required only over a single extended blade-passage region of the cascade. In addition, since analytic far-field solutions can be determined [14], the numerical solution domain can be restricted further to a single extended blade-passage region of finite extent in the axial-flow direction.

The Steady Background Flow

As a consequence of the assumption of uniform mean flow at inlet, the steady background flow will be isentropic and irrotational. Thus, $\mathbf{V} = \boldsymbol{\nabla}\Phi$,

$$\boldsymbol{\nabla} \cdot (\bar{\rho}\boldsymbol{\nabla}\Phi) = 0 \qquad (2.21)$$

12

and the fluid properties are related by

$$(M_{-\infty}A)^2 = \bar{\rho}^{\,\gamma-1} = (\gamma M_{-\infty}^2 P)^{(\gamma-1)/\gamma} = 1 - \frac{\gamma-1}{2}M_{-\infty}^2[(\nabla\Phi)^2 - 1]\,, \qquad (2.22)$$

where Φ, M, A, $\bar{\rho}$ and P are the steady velocity potential, Mach number, speed of sound propagation, density and pressure, respectively, and γ is the specific heat ratio of the fluid. Numerical procedures for determining two-dimensional steady potential flows through cascades have been developed extensively, e.g., see [15] and [16], particularly for flows with subsonic relative inlet and exit Mach numbers (i.e., $M_{\mp\infty} < 1$). The usual practice in such calculations is to solve the mass conservation equation (2.21), subject to a prescribed (i.e., $V_{-\infty}$ and $\Omega_{-\infty}$) uniform inflow, flow tangency at blade surfaces, and a Kutta condition at blade trailing edges.

The Linearized Unsteady Flow

The system of field equations that govern the linearized unsteady perturbation of a potential mean flow can be cast in a very convenient form by introducing the velocity decomposition [17, 18]

$$\mathbf{v} = \mathbf{v}_* + \nabla\phi = \mathbf{v}_R + \nabla\phi_* + \nabla\phi\,, \qquad (2.23)$$

where the rotational velocity, $\mathbf{v}_R$, is taken to be divergence-free far upstream of the blade row, ϕ_* is a convected or pressure-less potential (i.e., $\bar{D}\phi_*/Dt = 0$) which satisfies the condition $\nabla\phi_* \cdot \mathbf{n} = -\mathbf{v}_R \cdot \mathbf{n}$ at blade and wake mean positions, and the unsteady pressure depends only upon the potential, ϕ, through the relation $p = -\bar{\rho}\bar{D}\phi/Dt$, where $\bar{D}/Dt = i\omega + \nabla\Phi \cdot \nabla$ is a convective derivative based on the mean-flow velocity.

The system of field equations that governs the linearized unsteady flow variables, s, $\mathbf{v}_R$ and ϕ is determined by substituting the velocity decomposition (2.23) into the linearized Euler equations. If the underlying mean flow is isentropic and irrotational, the unsteady equations reduce to

$$\frac{\bar{D}s}{Dt} = 0 \qquad (2.24)$$

$$\frac{\bar{D}}{Dt}(\mathbf{v}_R - s\nabla\Phi/2) + [(\mathbf{v}_R - s\nabla\Phi/2)\cdot\nabla]\nabla\Phi = 0 \qquad (2.25)$$

and

$$\frac{\bar{D}}{Dt}\left(A^{-2}\frac{\bar{D}\phi}{Dt}\right) - \bar{\rho}^{\,-1}\nabla\cdot(\bar{\rho}\nabla\phi) = \bar{\rho}^{-1}\nabla\cdot(\bar{\rho}\mathbf{v}_*)\,. \qquad (2.26)$$

These equations are coupled only sequentially; hence, they can be solved in consecutively to determine the complex amplitudes of the entropy (s), rotational velocity ($\mathbf{v}_R$) and velocity potential (ϕ), respectively.

Closed form solutions [17, 19] can be determined for the entropy and rotational velocity fluctuations in terms of the known conditions at inlet, i.e.,

$$s(\mathbf{x}) = s_{-\infty}\exp(i\boldsymbol{\kappa}_{-\infty}\cdot\mathbf{X})\,, \qquad (2.27)$$

and

$$\mathbf{v}_R(\mathbf{x}) = [\nabla(\mathbf{X}\cdot\mathcal{A}_{-\infty}) + s_{-\infty}\nabla\Phi/2]\exp(i\boldsymbol{\kappa}_{-\infty}\cdot\mathbf{X}), \qquad (2.28)$$

13

where $\mathbf{X} = \Delta\mathbf{e}_T + \Psi\mathbf{e}_N$, Δ and Ψ are the drift and stream functions, respectively, of the steady background flow, and $\mathcal{A}_{-\infty} = \mathbf{v}_{R,-\infty} - s_{-\infty}\mathbf{V}_{-\infty}/2$ [19]. Since $\boldsymbol{\zeta}_{-\infty} = i\boldsymbol{\kappa}_{-\infty} \times \mathbf{v}_{R,-\infty}$ and the rotational velocity is divergence-free far upstream of the blade row, the vectors $\boldsymbol{\kappa}_{-\infty}$ and $\mathbf{v}_{R,-\infty}$ are orthogonal and $\mathbf{v}_{R,-\infty} = i(\boldsymbol{\kappa}_{-\infty} \times \boldsymbol{\zeta}_{-\infty})/|\boldsymbol{\kappa}_{-\infty}|^2$.

A convected potential of the form [18, 19]

$$\phi_* = \left[-i\omega^{-1}\mathcal{A}_{-\infty} \cdot \mathbf{V}_{-\infty} + F(\Psi)\right]\exp(i\boldsymbol{\kappa}_{-\infty} \cdot \mathbf{X}), \tag{2.29}$$

where

$$F(\Psi) = \frac{\omega^{-1}G\cos\Omega_{-\infty}(\boldsymbol{\kappa}_{-\infty} \times \mathcal{A}_{-\infty}) \cdot \mathbf{e}_z}{2\pi(1 - ia_0\omega)}\sin\left[\frac{2\pi[\Psi(\mathbf{x}) - \Psi(\mathbf{x}_-)]}{G\cos\Omega_{-\infty}}\right], \tag{2.30}$$

will ensure that $\mathbf{v}_* \cdot \mathbf{n} = (\mathbf{v}_R + \nabla\phi_*) \cdot \mathbf{n} = 0$ at the mean blade and wake surfaces, and hence, that $\nabla\phi \cdot \mathbf{n}$ is finite at such surfaces. Thus, the unsteady flow variables s, $\mathbf{v}_R$ and ϕ_* can be evaluated in terms of the drift and stream functions of the steady background flow.

The unsteady velocity potential, ϕ, is governed by the second-order partial differential equation, along with conditions at the blade and wake surfaces and at the inlet and exit boundaries. This function can be found numerically as a solution of the field equation (2.26) subject to the appropriate surface and far-field conditions. The flow tangency condition

$$\nabla\phi \cdot \mathbf{n} = [i\omega\mathbf{r} + (\nabla\Phi \cdot \boldsymbol{\tau})(\boldsymbol{\tau} \cdot \nabla)\mathbf{r} - (\mathbf{r} \cdot \nabla)\nabla\Phi] \cdot \mathbf{n} \tag{2.31}$$

applies at the mean blade surfaces (B_m), and the linearized unsteady pressure and normal velocity component are continuous across blade wakes (W_m), i.e.,

$$[\bar{D}\phi/Dt] = 0 \quad \text{and} \quad [\nabla\phi] \cdot \mathbf{n} = 0. \tag{2.32}$$

The velocity potential fluctuations in the far upstream and far downstream regions depend upon the prescribed excitation as well as on the acoustic and vortical response of the cascade. Analytic solutions for ϕ can be determined [14], which satisfy the requirements that acoustic response disturbances either attenuate with increasing axial distance from the blade row or propagate carrying energy away from or parallel to the blade row and that vorticity must be convected downstream. These solutions can be matched to a near-field numerical solution and thereby serve to complete the boundary-value problem for the unsteady potential. The vortical excitations determined by the wake analysis can thus be imposed at the inlet of a single extended blade passage of the FEGV, and the resultant acoustic response can be calculated. The amplitudes of the propagating acoustic response modes are then the targets of the active noise control analysis, which is presented in the next section.

3. Control Surface Analysis

The analyses in the previous two sections described how vortical and entropic excitations, that represent the effects of the rotor wakes on the stator row, are determined and how those excitations are used in the LINFLO analysis to determine the subsequent acoustic response of the stator row. The propagating far-field acoustic response waves thus found make up the discrete tone noise at multiples of the blade passing frequency, and are the targets of the control analysis given in this section. Note that for the purposes of the control analysis, all of the acoustic response waves are considered to be independent modes. The means, for instance, that the upstream and downstream moving acoustic response waves at 2 BPF are considered different, even though they both have the same frequency and interblade phase angle.

3.1 Anti-sound Generator Implementation

Wake/blade-row interaction noise can be reduced by using discrete blade surface actuators to generate sound out of phase with the undesired acoustic responses. These actuators, or pistons, have been implemented into the LINFLO analysis as oscillating control surfaces on the suction and pressure surfaces of each blade. A general blade motion is represented by Eq. (2.17). Control surfaces, that oscillate with a prescribed translational displacement normal to the mean blade surface with a given frequency and interblade phase angle, are defined over restricted portions of the blade surfaces. For a set of K control surfaces or pistons, the complex amplitude of the displacement at the reference ($m = 0$) blade is given by

$$\mathbf{r}_\mathbf{B}(\mathbf{x}) = \sum_{k=1}^{K} \mathbf{r}_k \left[U(\mathbf{x} - \mathbf{x}_{k,\text{le}}) - U(\mathbf{x} - \mathbf{x}_{k,\text{te}}) \right] \tag{3.1}$$

where the index k ranges over the K pistons, $\mathbf{r}_k = r_k \mathbf{e}_N$ is the displacement of the kth piston with complex amplitude r_k, $\mathbf{e}_N$ is a unit vector normal to the blade surface, U is the unit step function, and $\mathbf{x}_{k,\text{le}}$ and $\mathbf{x}_{k,\text{te}}$ are the locations of the leading and trailing edges of the kth piston. Individual pistons are specified by choosing midpoint locations and lengths as a fraction of chord. The control analysis then calculates chordwise positions of the leading and trailing edges of the piston, and requires the surface segment within this range to perform a translational oscillation at the specified frequency with the specified complex amplitude.

The analysis presented below shows how to determine the complex amplitudes $r_k, k = 1, \ldots, K$ of the pistons in order to best minimize the noise level, given the piston lengths and locations. The analysis assumes that there are K actuators on each blade, whose motions at each chordwise position are related to their counterparts on the reference blade through the interblade phase angle. An assessment of the effect of varying piston positions is given in the Results section.

3.2 Control Algorithm

The unsteady aerodynamic equations governing small unsteady perturbations of a uniform mean flow can be solved to yield the wavenumbers and attenuation constants for all

15

acoustic response disturbances [14]. The form of the acoustic response, i.e., the wavenumbers, attenuation constants, and propagation directions of each response wave, is independent of the means of excitation. The linearity of the unsteady equations for small amplitude excitations implies that superposition is valid, so if both an external excitation and a set of control surface oscillations act simultaneously, the net complex amplitudes of the acoustic response waves will be equal to the sum of the responses to the individual excitations. Thus, the control excitations can in principle be "tuned" so that their corresponding acoustic response waves are of equal amplitude but 180 degrees out of phase with the undesired responses produced by vortical and entropic excitations. Such surface motions then act as sources of anti-sound which cancel the undesired noise.

Assume that there are N acoustic response modes and K independent control surfaces. The total acoustic response due to both a specified excitation and a set of control surface motions will contain contributions attributable to each. The complex amplitudes of the net propagating acoustic response modes can therefore be expressed as a vector $\mathbf{p}_R$ such that

$$\mathbf{p}_R = \mathbf{p}_{R,\text{exc}} + \mathbf{p}_{R,\text{ctrl}} = \mathbf{p}_{R,\text{exc}} + \mathbf{Ar}. \tag{3.2}$$

The $N \times K$ matrix $\mathbf{A}$ contains as its elements the complex amplitudes of each propagating acoustic response wave resulting from a unit amplitude oscillation of each control surface, and the vector $\mathbf{r}$ contains the complex amplitudes r_k of the control surface motions. If $K = N$, the matrix $\mathbf{A}$ in this equation is square and invertible. Consequently, a set of control surface amplitudes given by

$$\mathbf{r}_{\text{exact}} = -\mathbf{A}^{-1}\mathbf{p}_{R,\text{exc}} \tag{3.3}$$

will yield $\mathbf{p}_R = 0$. In this case, the net amplitude of each propagating acoustic response wave will be zero.

If, however, $K < N$, then the length of the total response vector $\|\mathbf{p}_R\| = (\mathbf{p}_R^H \cdot \mathbf{p}_R)^{1/2}$ provides a natural measure of the net sound. In this expression, the superscript H denotes the Hermetian, or conjugate transpose, of the total response vector. In order to minimize $\|\mathbf{p}_R\|$ in a least-squares sense, it can be shown [20] that it is necessary to chose the vector $\mathbf{p}_{R,\text{ctrl}} = \mathbf{Ar}$ to be perpendicular to $\mathbf{p}_R$, i.e.,

$$\mathbf{p}_{R,\text{ctrl}}^H \cdot \mathbf{p}_R = (\mathbf{Ar})^H(\mathbf{Ar} + \mathbf{p}_{R,\text{exc}}) = 0. \tag{3.4}$$

Expanding the Hermetian product allows this equation to be written as

$$\mathbf{r}^H(\mathbf{A}^H\mathbf{Ar} + \mathbf{A}^H\mathbf{p}_{R,\text{exc}}) = 0 \tag{3.5}$$

whose nontrivial solution is given by

$$\mathbf{r}_{\text{lsq}} = -(\mathbf{A}^H\mathbf{A})^{-1}\mathbf{A}^H\mathbf{p}_{R,\text{exc}}. \tag{3.6}$$

This set of control surface motions will minimize the length of the acoustic response vector, $\|\mathbf{p}_R\|$.

The least squares minimization treats each element of the propagating response vector as equally important. It may be true in certain situations that the reduction of some modes is more important than others. Consequently, a weighting matrix $\mathbf{W}$ can be introduced into Eq. (3.2), i.e.,

$$\mathbf{W}\mathbf{p}_R = \mathbf{W}\mathbf{p}_{R,\text{exc}} + \mathbf{WAr}. \tag{3.7}$$

16

The matrix $\mathbf{W}$ is chosen to be square, diagonal, and composed of real elements. The values specified on the diagonal represent the relative importance assigned to the individual modes. The least-squares solution of this equation minimizes the length of a weighted net propagating response vector, $\|\mathbf{W}\mathbf{p}_R\|$, and is given by

$$\mathbf{r}_{\text{wlsq}} = -(\mathbf{A}^H \mathbf{W}^T \mathbf{W} \mathbf{A})^{-1} \mathbf{A}^H \mathbf{W}^T \mathbf{W} \mathbf{p}_{R,\text{exc}} . \tag{3.8}$$

Note that if the matrix $\mathbf{A}$ is invertible, then Eq. (3.8) reduces to the solution given in Eq. (3.3), and that the least squares solution given in Eq. (3.6) represents the case where the weighting matrix is chosen to be the identity matrix. Note also that this procedure minimizes the length of the weighted net propagating response vector, $\|\mathbf{W}\mathbf{p}_R\|$, which could result in a larger value for $\|\mathbf{p}_R\|$ itself than in the cases without control applied.

The conclusion, therefore, is that if there are more propagating acoustic response modes than available independent control surfaces, a natural measure of the net sound produced is provided by a scaled length of the total acoustic response vector. The scaling is provided through the use of a specified weighting matrix $\mathbf{W}$. The length of the scaled acoustic response vector is minimized by performing a least squares minimization procedure, whose result is given by Eq. (3.8), or by Eq. (3.6) if no weighting is performed.

3.3 Circumferentially Averaged Sound Pressure Level

The length of the total acoustic response vector $\|\mathbf{p}_R\|$ is directly related to the circumferentially averaged sound pressure level $\overline{\text{SPL}}$. The sound pressure level, SPL, is defined to be

$$\text{SPL} = 20 \log_{10} \frac{p_{\text{rms}}}{p_{\text{ref}}}, \tag{3.9}$$

where p_{rms} is the root mean square value of the unsteady pressure and p_{ref} is a reference pressure, whose dimensional value is generally taken to be 2×10^{-5} Pascals for airborne sound.

The mean-square pressure, $< \tilde{p}^2 > = p_{\text{rms}}^2$, for a pressure disturbance at frequency ω is defined to be

$$< \tilde{p}^2 > = \frac{1}{2\pi} \int_0^{2\pi} \tilde{p}^2 \, d(\omega t) \tag{3.10}$$

The acoustic response at a single frequency is composed of a series of individual modes with different wavenumbers, i.e.,

$$\tilde{p} = \text{Re}\{p \exp(i\omega t)\} = \text{Re}\left\{ \left(\sum_{n=-\infty}^{+\infty} p_n \right) \exp(i\omega t) \right\} \tag{3.11}$$

where the complex amplitude of the nth mode, p_n, can be expressed as

$$p_n = a_n \exp[\beta_n \xi + i(k_{\xi,n}\xi + k_{\eta,n}\eta)] \tag{3.12}$$

where $a_n, \beta_n, k_{\xi,n}$, and $k_{\eta,n}$ are the complex amplitude, attenuation constant, axial wavenumber, and circumferential wavenumber of the nth mode, respectively. Substituting Eq. (3.11) into Eq. (3.10) and performing the averaging results in

$$< \tilde{p}^2 > = \frac{1}{4} \sum_{n,m=-\infty}^{+\infty} (p_m p_n^* + p_n p_m^*) = \frac{1}{2} \sum_{n,m=-\infty}^{+\infty} \text{Re}\{p_n p_m^*\} \tag{3.13}$$

17

where the superscript * denotes the complex conjugate. The terms in Eq. (3.13) depend upon circumferential position, by Eq. (3.12). Therefore, taking the square root of $< \tilde{p}^2 >$ and substituting the result into Eq. (3.9) will result in a sound pressure level that is also dependent upon circumferential position. This dependence can be eliminated by averaging $< \tilde{p}^2 >$ around the circumference, i.e., integrating from $\eta = 0$ to $\eta = N_B G$, where N_B is the number of blades in the stator row, dividing by the circumference, and substituting the resulting expression into Eq. (3.9). This result is defined to be the circumferentially averaged sound pressure level, $\overline{SPL}$, which is given by

$$\overline{SPL} = 10 \log_{10} \left(\sum_{n=-\infty}^{+\infty} \frac{1}{2} p_n p_n^* \right) - 20 \log_{10} p_{ref} \tag{3.14}$$

where the overbar indicates circumferential averaging.

As above, consider the case where there are N propagating acoustic response modes. If the complex amplitudes of the propagating response modes are placed in a vector $\mathbf{p}_R$, then the argument to the logarithm in Eq. (3.14) is related to the magnitude of this vector via

$$\sum_{N \text{ prop}} \frac{1}{2} p_{R,n} p_{R,n}^* = \frac{1}{2} \mathbf{p}_R^H \mathbf{p}_R = \frac{1}{2} ||\mathbf{p}_R||^2. \tag{3.15}$$

The logarithm is a monotonically increasing function, so the minimum of its argument corresponds to the minimum of $\overline{SPL}$. Consequently, since the least squares solution for the control surface motions given in Eq. (3.6) minimizes $||\mathbf{p}_R||$, it also minimizes $\overline{SPL}$.

In summary, given N propagating acoustic response modes and K independent control surfaces, then if $K = N$ the oscillation amplitudes of the pistons can be determined using Eq. (3.3) to give complete cancellation of the noise. If $K < N$, then the magnitude of the net propagating acoustic response vector provides a convenient measure of the net sound, and can be minimized by using the least squares minimization procedure given in Eq. (3.6) or the weighted least squares minimization procedure given in Eq. (3.8). The least squares minimization procedure also minimizes the circumferentially averaged sound pressure level, $\overline{SPL}$.

4. Results

The following results are based on an analysis of a representative fan stage composed of an upstream fan rotor and a downstream fan exit guide vane. The FEGV blades are constructed by superimposing the thickness distribution of a NACA 0008 airfoil on a circular arc camber line. The latter has a height at blade midchord of 0.08. The FEGV cascade has a gap to chord ratio G of 0.836, and a stagger angle Θ of 10 deg. The inlet and exit relative freestream Mach numbers are $M_{-\infty} = 0.55$ and $M_{+\infty} = 0.45$, respectively, and the inlet and exit flow angles are $\Omega_{-\infty} = 30$ deg and $\Omega_{+\infty} = -2.39$ deg respectively. The rotor blade passing frequency (BPF) as seen from the stator is $\omega = 4.106$, and the interblade phase angle at BPF is $\sigma = -2.513$.

The chord length of the fan blades is approximately 2.3 times the chord of the FEGV blades. The gap to chord ratio G' of the fan cascade is 2.09. The wheel speed at the radial location chosen for the 2D cascade section is 1.366, nondimensionalized with respect to the inlet flow velocity of the response row. This set of parameters results in an exit flow angle for the rotor row of $\Omega'_{+\infty} = -45$ deg.

4.1 Generation

The wake model given in Section 2.1 was used to compute the velocity distribution downstream of the rotor. A Fourier decomposition of this velocity field was then performed to determine the Fourier components of the unsteady excitation at the FEGV inlet. The magnitudes of the v_n^+ components were evaluated at the leading edges of the stator blades. This location is two (rotor) blade chords downstream of the fan. Table 4.1 shows the chosen v_n^+ values, along with the frequencies and interblade phase angles for the first three harmonics of the blade passing frequency. The analysis in Section 2.1 showed how the vortical disturbance amplitudes could be used to determine the amplitude of entropic disturbances as well, but the entropic disturbances at these amplitudes do not produce significant acoustic responses and are therefore not shown.

An analysis of the equations governing the unsteady flow in the far-field of the stator reveals that at BPF, the acoustic response is "cut-off," i.e., all of the acoustic waves present in the flow are of the decaying type. At 2 BPF, there are two propagating response waves,

Vortical Excitation Data

n	σ_n	ω_n	v_n^+
1	-2.513	4.106	$(.14807 \times 10^{-1}, 0.)$
2	-5.026	8.212	$(.82745 \times 10^{-2}, 0.)$
3	-7.539	12.318	$(.41493 \times 10^{-2}, 0.)$

Table 4.1: Interblade phase angles, frequencies, and complex amplitudes for the first three harmonics of the vortical excitation calculated from the wake model.
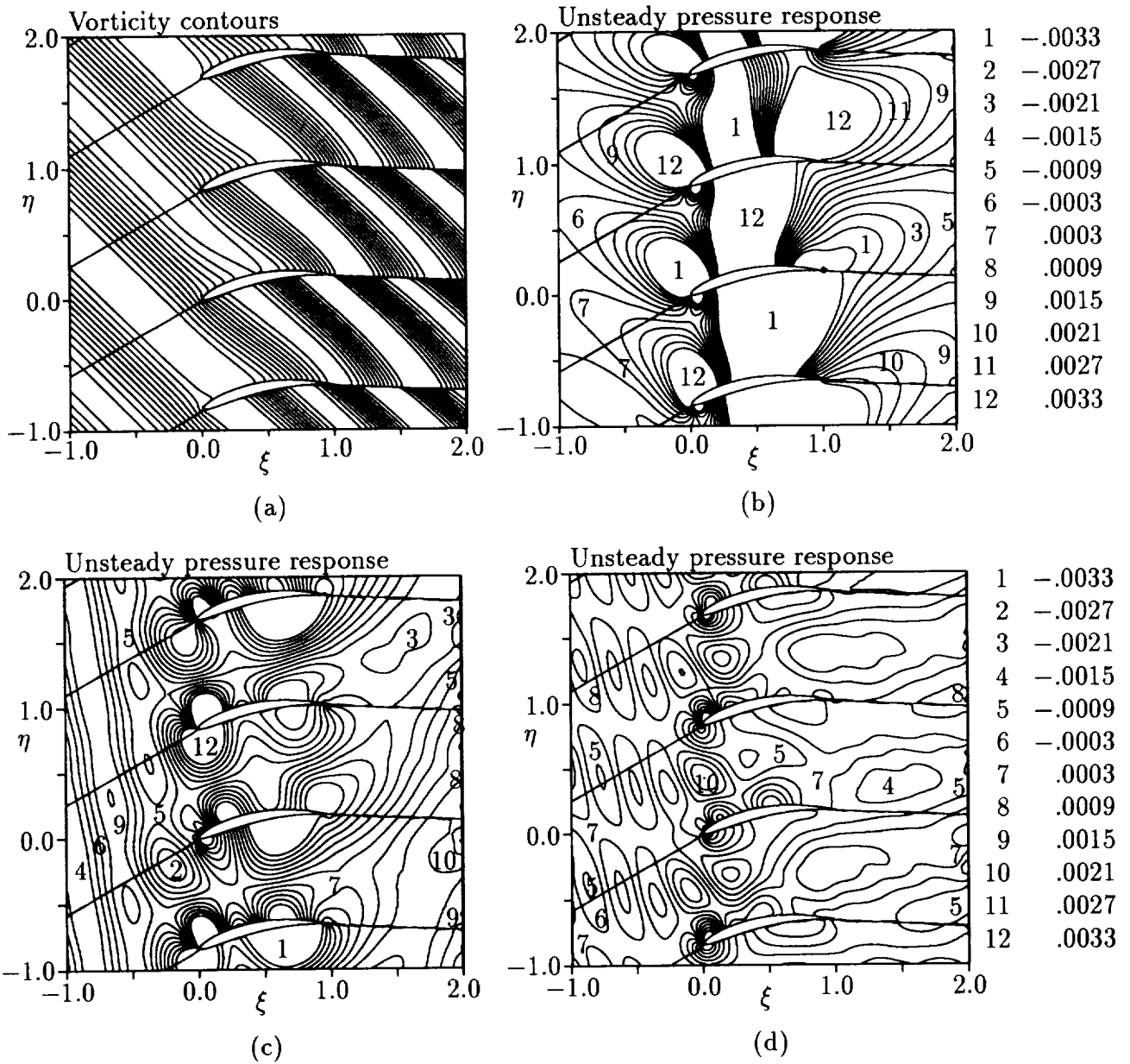
19

Figure 4.1: Vortical excitation and acoustic response fields. (a) vortical field at BPF; acoustic fields at (b) BPF, (c) 2 BPF, and (d) 3 BPF.

one in the upstream flow field and one in the downstream field, and at 3 BPF, there are four propagating response waves, with two in each flow field.

Figure 4.1 shows contours of the real part of the unsteady vorticity field at BPF, and contours of the real part of the unsteady pressure at BPF, twice BPF, and three times BPF. The vortical fields at twice and three times BPF are similar to that at BPF, with slightly different shapes to the contours. These contour plots are the results of a numerical solution of the equations governing the steady and the first-order unsteady flows. In each case, vortical excitations have been imposed at the inlet to the cascade. The vorticity in Fig. 4.1a is convected through the blade row by the steady background flow. For the acoustic

20

response fields, the contour ranges were chosen to emphasize the propagating acoustic modes. Note that in the BPF acoustic contour plot shown in Fig. 4.1b, all the response modes are decaying, so the magnitude of the unsteady pressure drops quickly with increasing distance from the blade row.

The pressure contours for the 2 BPF case in Fig. 4.1c show a single propagating wave upstream of the cascade and a single propagating wave downstream of the cascade. If all propagation angles are measured counterclockwise from the positive ξ axis. The upstream acoustic wave is propagating at an angle of -170.8 deg and has a wavelength of 0.676 blade chords, while the downstream acoustic wave is propagating at an angle of -27.8 deg and has a wavelength of 1.98 blade chords. The complex amplitude of the upstream propagating wave is $p_{R,-\infty} = (-0.1309 \times 10^{-2}, 0.4937 \times 10^{-3})$, and the complex amplitude of the downstream propagating wave is $p_{R,+\infty} = (0.1970 \times 10^{-2}, -0.2540 \times 10^{-3})$.

The 3 BPF acoustic field shows two propagating waves in each flow field. The upstream waves are propagating at angles of 172.8 deg and -156.5 deg, and have wavelengths of 0.52 and 0.42 blade chords, respectively. The downstream waves are propagating at angles of 18.7 deg and -79.0 deg, and have wavelengths of 1.33 and 1.03 blade chords. The complex amplitudes of these propagating waves are

$$
\begin{aligned}
p_{R,-\infty,1} &= (0.2065 \times 10^{-3}, & 0.4054 \times 10^{-3}) \\
p_{R,-\infty,2} &= (-0.5222 \times 10^{-3}, & -0.3309 \times 10^{-3}) \\
p_{R,+\infty,1} &= (0.1135 \times 10^{-3}, & 0.2421 \times 10^{-3}) \\
p_{R,+\infty,2} &= (0.8927 \times 10^{-3}, & 0.2673 \times 10^{-3})
\end{aligned}
\tag{4.1}
$$

A linear superposition of two acoustic waves of equal magnitude and different propagation directions results in a series of ellipses on a contour plot of the unsteady pressure. The magnitudes of the upstream propagating waves at 3 BPF are relatively close to each other (a factor of approximately 1.36), and the angle between them is approximately 30 degrees. The acoustic field in Fig. 4.1d reflects this by showing somewhat elongated ellipses upstream of the cascade. The downstream flow field is dominated by the $n = 2$ mode, which is much larger in magnitude (by a factor of about 3.5) than the downstream $n = 1$ mode, and the contour plot shows this as well.

4.2   Control

Complete Cancellation

The control procedures described in Section 3 have been implemented for the representative fan stage. The acoustic responses at 2 BPF and 3 BPF contain propagating acoustic response waves with the complex amplitudes given above. To demonstrate the possibility of complete cancellation of the propagating acoustic modes, at each multiple of BPF the number of control surfaces was chosen to be equal to the known number of propagating acoustic response modes. For this demonstration, the lengths of all of the control surfaces was chosen to be 0.1 chord. The locations of the control surfaces were specified arbitrarily, and as long as non-overlapping control surfaces were selected, the resulting control matrix $\mathbf{A}$ in Eq. (3.3) could be inverted. The elements of $\mathbf{A}$ were determined by specifying a unit
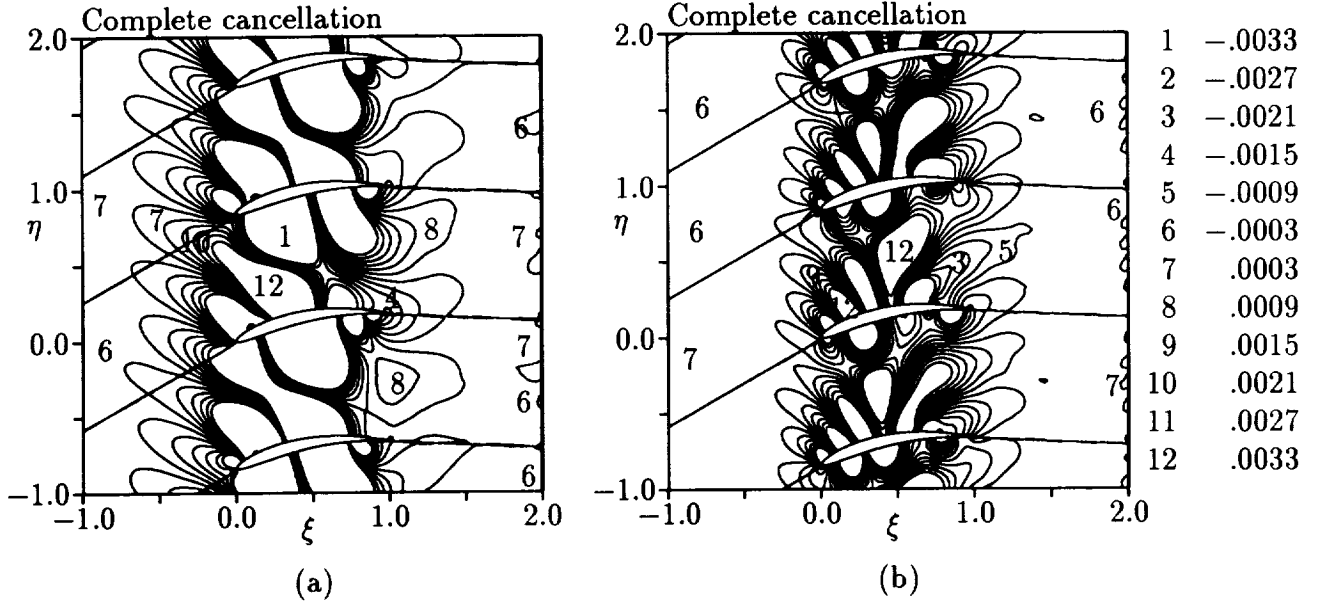
Figure 4.2: Acoustic fields showing complete cancellation of propagating modes at (a) 2 BPF and (b) 3 BPF.

amplitude displacement for each control surface as an excitation for the LINFLO analysis, and calculating the resulting complex amplitudes of each of the propagating response modes.

Since two propagating acoustic response modes exist at 2 BPF, two control surfaces (on each blade) were selected. One piston was placed on the suction surface centered at 0.2 chord; the other, on the pressure surface at 0.8 chord. The solution of Eq. (3.3) for the 2 BPF excitation gave the complex amplitudes of the control surface motions as $r_1 = (0.2542 \times 10^{-3}, -0.4153 \times 10^{-3})$ and $r_2 = (-0.1224 \times 10^{-2}, 0.1080 \times 10^{-2})$.

Four control surfaces were used for the 3 BPF case, two of which were placed on each surface of the blade. The control surfaces on the suction surface were centered at 0.2 and 0.7 chord; those on the pressure surface, at 0.3 and 0.8 chord. The solution to Eq. (3.3) for the responses in the propagating modes to the vortical excitation and to unit amplitude piston oscillations yields

$$
\begin{aligned}
r_1 &= (0.4286 \times 10^{-4}, \quad 0.9962 \times 10^{-4}) \\
r_2 &= (0.9207 \times 10^{-5}, \quad 0.1902 \times 10^{-3}) \\
r_3 &= (0.2665 \times 10^{-3}, \quad 0.6581 \times 10^{-4}) \\
r_4 &= (-0.4100 \times 10^{-4}, \quad 0.1854 \times 10^{-3})
\end{aligned}
\tag{4.2}
$$

for the complex amplitudes of the control surface motions. The magnitudes of the acoustic response modes when both the vortical excitation and the control surface motions were present were all on the order of 10^{-7}. Contour plots of the acoustic fields with the control motions applied along with the vortical excitation are shown in Fig. 4.2. The response within the cascade in these figures is dramatically larger than that without the control motions, but the far field acoustic response has been virtually eliminated. No other structural or aerodynamic effects that may arise due to the piston motions have been evaluated. Should difficulties arise, however, the control analysis can be performed with the pistons at alternate locations. The effect of piston location on the control effectiveness is examined below.

Since there are a finite number of grid nodes on the surfaces of the blades, the calculated leading and trailing edges of the piston did not fall directly upon grid points. The length of the piston as seen by the numerical analysis, therefore, was not exactly equivalent to the length specified, and a small change in the location of the midpoint of the piston for a given length yielded differing numbers of included gridpoints. This is an inevitable consequence of the non-uniform distribution of mesh points along the blade surface. The numerical length of the piston thus seen by the numerical code appeared to increase and decrease as it was moved along the blade, even though the specified length was not intended to change. The numerical representation of the piston thus implies that its specified length and location are not completely independent. This complicates parametric studies of the effects of changing lengths or locations of the control surfaces. Also to be noted is that the surface boundary condition contained in Eq. (2.31) contains the gradient of the displacement. The pistons have finite length, so their designated motions take the form of square pulses of translational oscillations of a given complex amplitude. The numerical implementation, however, performs a second-order central difference of the displacement on an irregular mesh, which has the effect of rounding the corners of the specified displacement. Neither of these effects, i.e., the weak coupling of piston length and location by the surface grid nodes, and the finite difference smoothing of the specified displacements, dramatically affect the control analysis. Rather, these factors are endemic to the numerical formulation, and make the results somewhat dependent on the density of the grid points on the surfaces of the blades. Each of the cases presented here was run on a global mesh containing 155 streamwise points and 40 circumferential points, which distributed 65 points on each of the suction and pressure surfaces of the blades. The number of surface grid points contained within the 0.1 length pistons ranged from four to seven, depending on location.

To ascertain the effect of varying the control surface locations, a series of 50 tests was run at 3 BPF. In each case, a piston of length 0.1 was placed at varying locations on either the suction or pressure surface of each FEGV blade, and oscillated at unit amplitude. Twenty-five top and twenty-five bottom surface locations were examined. The magnitude of the acoustic response of each propagating mode is shown as a function of the piston location in Fig. 4.3. Fig. 4.3a contains information from moving the piston along the suction surface, while Fig. 4.3b contains information from moving the piston along the pressure surface. There are four propagating modes at this frequency and interblade phase angle, so four lines appear on each figure.

An examination of Fig. 4.3 suggests several conclusions. First, it appears that there are no obviously preferred locations for the pistons. Each mode has a completely different reaction to variations in piston location, and while the curves do show maxima, the maximum response value of each curve occurs at a different piston location. Second, the figure shows a certain jaggedness in some of the response magnitude curves. This effect is due to the weak coupling between length and location described above. Third, since each propagating mode has a unique dependence upon piston location, any conclusions made on piston location would be case dependent. While a complex optimization could in principle be performed to find a set of piston locations that would minimize the necessary control amplitudes, it is unlikely that the resulting set of locations could be generalized to arbitrary cases. Finally,
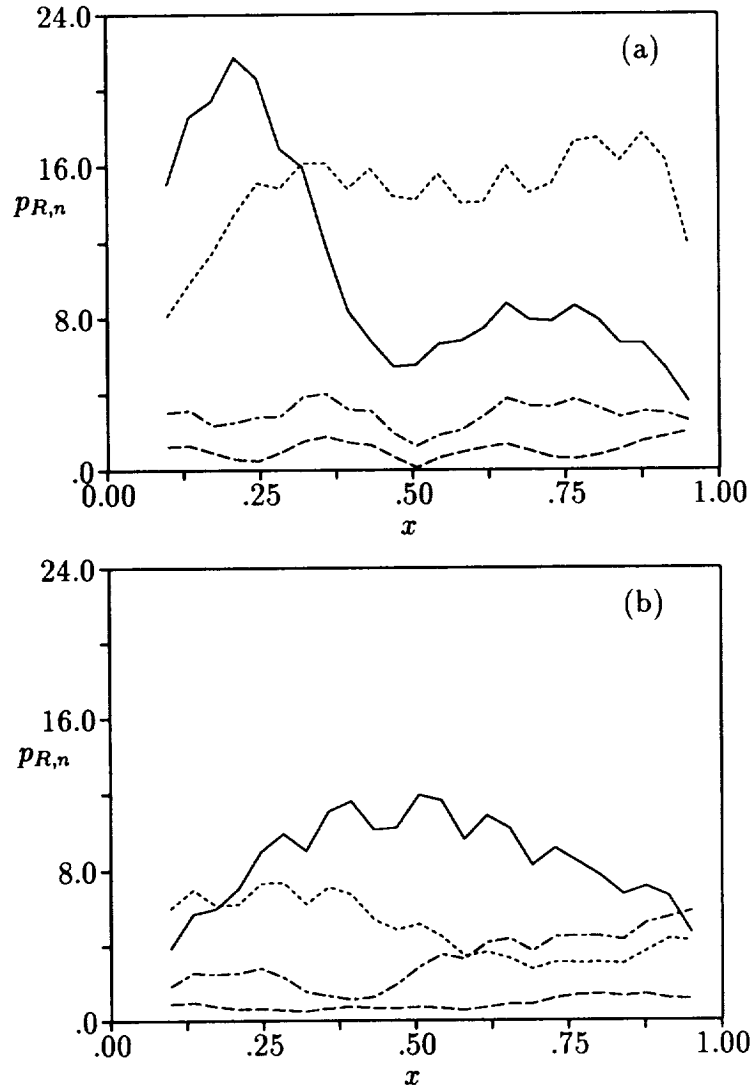
Figure 4.3: Effect of piston placement on mode magnitudes. (a) Suction surface piston, (b) Pressure surface piston. In each case, the solid line is for mode 1 upstream, the short dashes are for mode 2 upstream, the mixed long and short dashes is for mode 1 downstream, and the long dashes are for mode 2 downstream.

the acoustic response modes generally have only a limited dependence on actuator location. The greatest dependence observed in this study occurred for the $n = 1$ upstream mode, which varies in magnitude by only a factor of three when the piston is moved along the suction surface. It would seem, therefore, that no "rule of thumb" conclusions about piston placement can be drawn, and that while an optimization of locations could be performed, the resulting improvement in control displacements is not likely to be dramatic.

24

To illustrate the effects of the least squares minimization solution given in Eq. (3.6) and the weighted least squares solution given in Eq. (3.8), consider the same 3 BPF case as above, which contains four propagating acoustic response waves. Assume now that there are only two pistons available for control. The two pistons selected for demonstration of the least squares concept are the ones used to achieve complete cancellation for the 2 BPF excitation. Recall that in that case, the pistons each had length 0.1, and were centered at $x = 0.2$ on the suction surface and $x = 0.8$ on the pressure surface, respectively.

The least squares minimization is applied by solving Eq. (3.6), which yields the complex amplitudes $r_1 = (-0.4830 \times 10^{-5}, -0.4022 \times 10^{-4})$ and $r_2 = (-0.7891 \times 10^{-4}, -0.8567 \times 10^{-5})$. The acoustic contours for this case are shown in Fig. 4.4a. With the control applied, the changes in the magnitudes of each propagating response wave are shown in Table 4.2. The magnitude of the net propagating response vector $\|p_R\|$ has been reduced by approximately 28.4% overall, which corresponds to a decrease in the circumferentially averaged SPL of about 3 dB.

To demonstrate the weighted least squares minimization procedure, a weighting matrix is chosen to require complete cancellation of both downstream modes. The required control displacements for this case are then $r_1 = (-0.5216 \times 10^{-3}, 0.3196 \times 10^{-3})$ and $r_2 = (-0.2631 \times 10^{-3}, 0.2343 \times 10^{-3})$. Acoustic contours for this case are shown in Fig. 4.4b. Note that the downstream flow field is completely quiet, while the upstream response has been increased significantly. The results are summarized in Table 4.3.

These results are dramatic, in that, although the downstream acoustic response waves have been virtually eliminated, the magnitudes of the upstream response waves have increased by almost two orders of magnitude. An examination of Fig. 4.3 reveals the reason for the strong upstream response. In the figure, it is clear that the downstream acoustic response waves have uniformly lower magnitudes than the upstream response waves, when excited by a unit amplitude control excitation. Consequently, a relatively large control displacement is required to achieve a large enough response to cancel the undesired downstream modes. This large control surface displacement is then multiplied by the far greater sensitivity of the upstream modes to yield a strong upstream response.

Leasts Squares Minimization

3 BPF with 2 Pistons

Magnitudes of Each Propagating Acoustic Response Mode, $\|p_{R,n}\|$

n	No control	Control	Percent Change
1	0.4550×10^{-3}	0.2738×10^{-3}	-39.8%
2	0.6182×10^{-3}	0.3931×10^{-3}	-36.4%
3	0.2674×10^{-3}	0.2872×10^{-3}	$+7.40\%$
4	0.9319×10^{-3}	0.6876×10^{-3}	-26.2%

Table 4.2: Least squares minimization of the net acoustic response, with four propagating acoustic response modes and only two control surfaces.
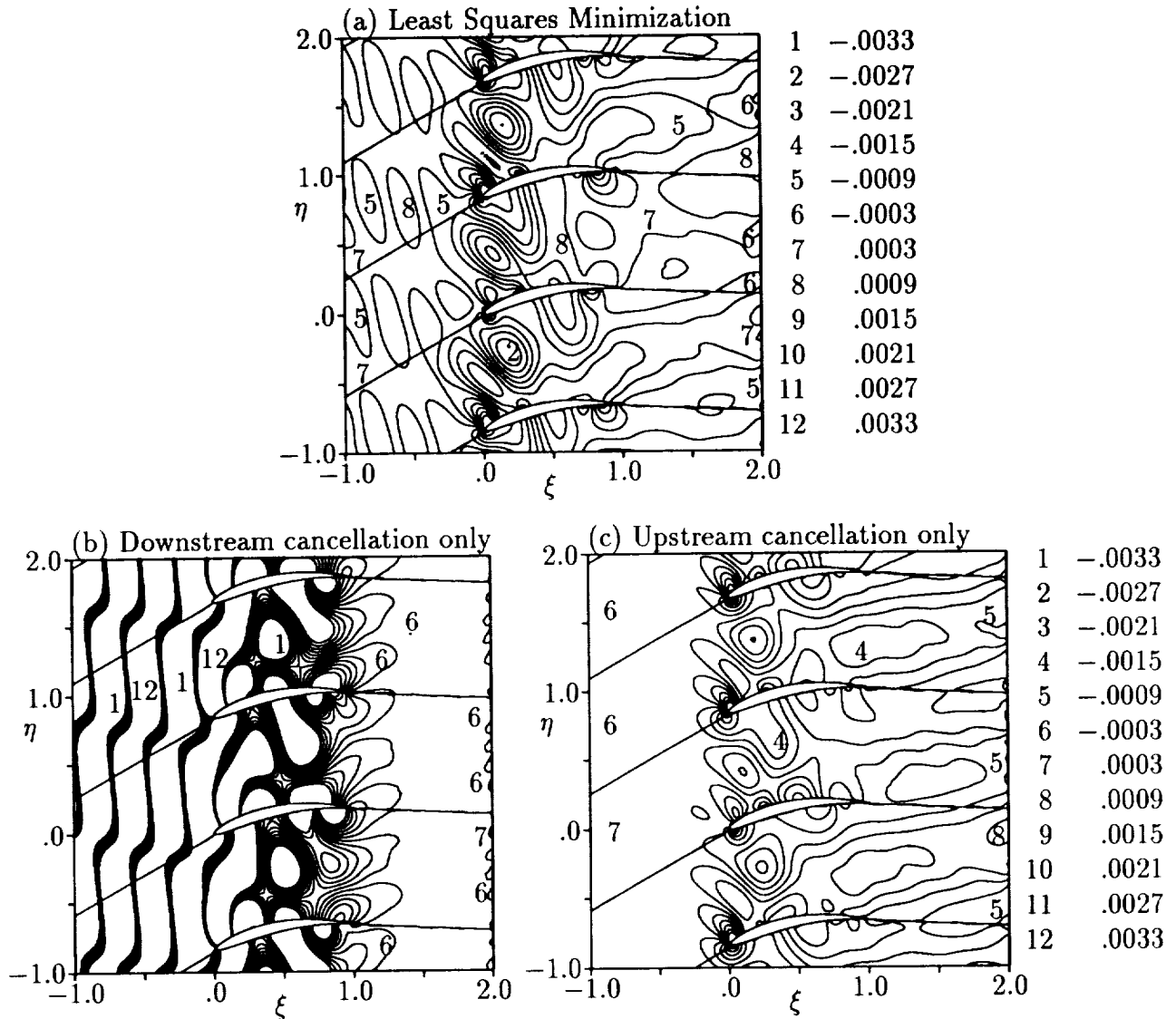
Figure 4.4: Weighted least squares minimizations. (a) Least squares solution with two pistons and four modes. (b) Downstream cancellation only. (c) Upstream cancellation only.

This suggests that if the weighting matrix is chosen so that only the upstream modes are cancelled rather than the downstream modes, the overall result will not be as severe. Application of the control analysis reveals that this is indeed the case, and acoustic contours for this case are shown in Fig. 4.4c. The required control displacements are $r_1 = (-0.1293 \times 10^{-4}, -0.3205 \times 10^{-4})$ and $r_2 = (-0.3094 \times 10^{-4}, 0.3616 \times 10^{-4})$, and the changes in the response modes are shown in Table 4.4. The upstream response modes respond more readily to the control, and this is reflected in the fact that even though the downstream modes were ignored in the weighted analysis in this case, one of them actually decreased in magnitude by almost 25%.

The conclusion to be drawn, therefore, is that in each case where control is to be applied and there are not enough pistons available for complete cancellation, it is important to

Weighted Leasts Squares Minimization

3 BPF with 2 Pistons

Downstream Cancellation Only

Magnitudes of Each Propagating Acoustic Response Mode, $\|p_{R,n}\|$

n	No control	Control	Percent Change
1	0.4550×10^{-3}	0.1404×10^{-1}	$+2986\%$
2	0.6182×10^{-3}	0.8098×10^{-2}	$+1210\%$
3	0.2674×10^{-3}	0.2066×10^{-6}	-99.92%
4	0.9319×10^{-3}	0.3232×10^{-6}	-99.97%

Table 4.3: Weighted least squares minimization cancelling the downstream acoustic response modes.

Weighted Leasts Squares Minimization

3 BPF with 2 Pistons

Upstream Cancellation Only

Magnitudes of Each Propagating Acoustic Response Mode, $\|p_{R,n}\|$

n	No control	Control	Percent Change
1	0.4550×10^{-3}	0.1165×10^{-6}	-99.95%
2	0.6182×10^{-3}	0.2156×10^{-6}	-99.97%
3	0.2674×10^{-3}	0.2001×10^{-3}	-24.98%
4	0.9319×10^{-3}	0.9989×10^{-3}	$+7.190\%$

Table 4.4: Weighted least squares minimization cancelling the upstream acoustic response modes.

examine the behavior of each propagating acoustic response mode to the control.

5. Conclusions

This report presents a combined analytical/computational investigation of sound generation in cascades, and the subsequent active control of the acoustic responses through the use of blade-surface actuators. To ascertain the proper dimensional magnitudes of representative acoustic response, an existing fan wake model was analyzed to determine appropriate unsteady vortical and entropic excitations to a downstream FEGV. The magnitudes of the excitations depend upon the geometry of the fan stage, the wheel speed and exit mean flow of the rotor, and the shape, centerline velocity defect, and half-width of the rotor wakes. Examples of the generation of acoustic response waves were presented by applying vortical excitations at the inlet of the FEGV, and solving the governing steady and first-order unsteady flow equations numerically using the LINFLO analysis.

At a given frequency and interblade phase angle the form of the acoustic response of the FEGV, i.e., the wavenumbers, attenuation constants, and propagation directions of the far-field acoustic response waves, is independent of the means of excitation. Therefore, the acoustic responses due to a set of control surface oscillations on the FEGV blades are of the same form as those due to an external excitation. The complex amplitudes of the control surface motions can be related to the complex amplitudes of the undesired propagating acoustic response waves through a set of simultaneous linear equations. If the number of available control surfaces is equal to the number of propagating acoustic response waves, this system of equations can be solved exactly, resulting in a set of control displacements that completely cancel the noise. Examples of complete cancellation at twice and three times BPF were shown.

If the number of acoustic response waves exceeds the number of control surfaces, then the magnitude of a net propagating acoustic response vector provides a convenient measure of the effectiveness of the control. A least squares minimization procedure minimizes this quantity, which is directly related to the circumferentially averaged sound pressure level. A weighting matrix has also been incorporated into the control analysis, to allow selective cancellation of the acoustic response waves. An example of the least squares minimization procedure was presented, as well as cases where the noise was completely eliminated in either the upstream or the downstream flowfield of the FEGV.

The magnitude of each propagating acoustic response wave has a unique dependence upon piston location. Consequently, no clear "rule of thumb" exists for piston placement, which is therefore case dependent. A degree of relative insensitivity of some of the modes to piston location was also observed in the cases studied, which implies that a complex optimization procedure to determine the piston locations that lead to minimum required control displacents is not likely to result in a dramatic improvement.

28

References

[1] Groeneweg, J. F. and Rice, E. J., "Aircraft Turbofan Noise," *Transactions of the ASME: Journal of Turbomachinery*, Vol. 109, January 1987, pp. 130–141.

[2] Ffowcs Williams, J., "Anti-sound," *Proceedings of the Royal Society of London, Series A*, Vol. 395, 1984, pp. 63–88.

[3] Koopmann, G. and Fox, D., "Active Source Cancellation of the Blade Tone Fundamental and Harmonics in Centrifugal Fans," *Journal of Sound and Vibration*, Vol. 126, No. 2, 1988, pp. 209–220.

[4] Burgess, J., "Active Adaptive Sound Control in a Duct: A Computer Simulation," *Journal of the Acoustic Society of America*, Vol. 70, September 1981, pp. 715–726.

[5] Cunefare, K. and Koopman, G., "Global Optimum Active Noise Control: Surface and Far Field Effects," *Journal of the Acoustic Society of America*, Vol. 90, 1991, pp. 365–373.

[6] Meirovitch, L. and Thangjitham, S., "Active Control of Sound Radiation Pressure," *Transactions of the ASME: Journal of Vibration, Acoustics, Stress and Reliability in Design*, Vol. 112, 1990, pp. 237–244.

[7] Neise, W. and Koopmann, G., "Active Sources in the Cutoff of Centrifugal Fans to Reduce the Blade Tones at Higher-Order Duct Mode Frequencies," *Transactions of the ASME: Journal of Vibration and Acoustics*, Vol. 113, January 1991, pp. 123–131.

[8] Thomas, R., Burdisso, R., Fuller, C., and O'Brien, W., "Active Control of Fan Noise from a Turbofan Engine," Paper 93–0597, AIAA, 1993.

[9] Simonich, J., Lavrich, P., Sofrin, T., and Topol, D., "Active Aerodynamic Control of Wake-Airfoil Interaction Noise - Experiment," In *Proceedings of the DGLR/AIAA 14th Aeroacoustics Conference*, pp. 229–237, May 1992, DGLR/AIAA Paper No. 92-02-038.

[10] Verdon, J. M., "Unsteady Aerodynamic Methods for Turbomachinery Aeroelastic and Aeroacoustic Applications," Paper AIAA-92-0011, AIAA 30th Aerospace Sciences Meeting, Reno, Nevada, January 1992.

[11] Verdon, J., Barnet, M., Hall, K., and Ayer, T., "Development of Unsteady Aerodynamic Analyses for Turbomachinery Aeroelastic and Aeroacoustic Applications," Technical report, NASA Contractor Report 4405, October 1991.

[12] Manwaring, S. R. and Fleeter, S., "Forcing Function Effects on Rotor Periodic Aerodynamic Response," *Transactions of the ASME: Journal of Turbomachinery*, Vol. 113, April 1991, pp. 312–319.

[13] Majjigi, R. K. and Gliebe, P. R., "Development of a Rotor Wake/Vortex Model," CR 174849, NASA, 1984.

[14] Verdon, J. M., "The Unsteady Flow in the Far Field of an Isolated Blade Row," *Journal of Fluids and Structures*, Vol. 3, No. 2, March 1989, pp. 123–149.

[15] Caspar, J. R., "Unconditionally Stable Calculation of Transonic Potential Flow Through Cascades Using an Adaptive Mesh for Shock Capture," *Transactions of the ASME: Journal of Engineering for Power*, Vol. 105, No. 3, July 1983, pp. 504–513.

[16] Whitehead, D. S. and Newton, S. G., "A Finite Element Method for the Solution of Two-Dimensional Transonic Flows in Cascades," *International Journal for Numerical Methods in Fluids*, Vol. 5, No. 2, February 1985, pp. 115–132.

[17] Goldstein, M. E., "Unsteady Vortical and Entropic Distortions of Potential Flows Round Arbitrary Obstacles," *Journal of Fluid Mechanics*, Vol. 89, No. Part 3, December 1978, pp. 433–468.

[18] Atassi, H. M. and Grzedzinski, J., "Unsteady Disturbances of Streaming Motions around Bodies," *Journal of Fluid Mechanics*, Vol. 209, December 1989, pp. 385–403.

[19] Hall, K. C. and Verdon, J. M., "Gust Response Analysis for Cascades Operating in Nonuniform Mean Flows," *AIAA Journal*, Vol. 29, No. 9, September 1991, pp. 1463–1471.

[20] Strang, G., *Linear Algebra and Its Applications*. Academic Press, New York, NY, 1980.

List of Symbols

All physical parameters listed below are dimensionless. Lengths have been scaled with respect to blade chord, time with respect to the ratio of blade chord to upstream freestream flow speed, density with respect to its upstream freestream value, velocity with respect to the upstream freestream flow speed, and entropy with respect to the fluid specific heat at constant pressure. The number(s) in parentheses at the end of each symbol description indicates an equation in which the symbol appears.

Roman

$\mathcal{A}_{-\infty}$	Constant vector, (2.28).
A	Speed of sound propagation in steady background flow.
$\mathbf{A}$	Coefficient matrix in control equations.
a_0	Constant, (2.30).
$\mathcal{B}$	Moving blade surface.
B	Blade mean position.
C_D	Section drag coefficient, (2.9).
$\mathbf{e}$	Unit vector.
F	Complex function of mean-flow stream function, (2.30).
$f(N')$	Wake profile shape function, (2.7).
$\mathbf{G}$	Cascade gap vector ($= G\mathbf{e}_\eta$), Fig. 2.1.
$\tilde{H}_T$	Total enthalpy, (2.13).
H_T	Total enthalpy in steady background flow.
$\tilde{H}$	Static enthalpy, (2.13)
H	Static enthalpy in steady background flow.
i	Imaginary unit.
K	Number of control surfaces per blade.

k_ξ, k_η	Axial and circumferential wave numbers.
M	Mach number in steady background flow.
m	Blade number index
$\tilde{P}$	Pressure.
P	Pressure in steady background flow.
$\tilde{p}$	First-order unsteady pressure.
p	Complex amplitude of first-harmonic unsteady pressure.
$\mathbf{p}_R$	Vector containing complex amplitudes of the propagating acoustic response waves.
p_{rms}	Root mean square pressure, (3.9)
$\mathcal{R}$	Surface (blade or wake) displacement vector, (2.17).
$\mathbf{r}$	Complex amplitude of surface (blade or wake) displacement vector, (2.17); vector of complex amplitudes of actuator displacements, (3.1).
r_k	Complex amplitude of displacement of kth actuator.
$\tilde{s}$	First-order unsteady entropy, (2.14).
s	Complex amplitude of first-harmonic unsteady entropy, (2.16).
SPL	Sound pressure level, (3.9).
t	Time.
(T', N')	Coordinates tangential and normal to the exit flow direction of the rotor.
u^+, v^+	Components of perturbation velocity in Fig. 2.2 tangential and normal to the inlet mean flow velocity of the stator.
$\tilde{\mathbf{V}}$	Velocity.
$\mathbf{V}$	Velocity in steady background flow.
$\tilde{\mathbf{v}}$	First-order unsteady velocity.

$\mathbf{V}_W$	Wheel velocity of rotor, $= V_W \mathbf{e}_{\eta'}$, Fig. 2.1
V_{def}	Wake velocity defect, (2.6)
V_e	Magnitude of wake edge velocity, (2.11)
V_{min}	Minimum wake velocity, (2.6)
$\mathbf{v}$	Complex amplitude of first-harmonic unsteady velocity.
$\mathbf{v}_R$	Complex amplitude of first-harmonic rotational unsteady velocity.
$\mathbf{v}_*$	Complex amplitude of first-harmonic source-term unsteady velocity.
$\mathcal{W}$	Moving wake surface.
W	Wake mean position.
$\mathbf{W}$	Weighting matrix for control equations, (3.7)
$\mathbf{X}$	Lagrangian coordinate vector.
$\mathbf{x}$	Position vector.
x, y	Cartesian coordinates along and normal to mean position of blade chord, Fig. 2.1.

Greek

β	Acoustic attenuation constant.
γ	Fluid specific heat ratio.
Δ	Drift function.
δ	Wake half-width, (2.10)
$\tilde{\zeta}$	First-order unsteady vorticity.
ζ	Complex amplitude of first-harmonic unsteady vorticity.
Θ	Cascade stagger angle, Fig. 2.1.
κ	Wave number vector.

ξ, η	Cascade axial and circumferential Cartesian coordinates, Fig. 2.1.
$\tilde{\rho}$	Density.
$\bar{\rho}$	Density in steady background flow.
$\hat{\rho}$	First-order unsteady density.
σ	Interblade phase angle.
τ	Unit tangent vector, (2.31).
Φ	Velocity potential for inviscid steady background flow.
$\tilde{\phi}$	Velocity potential for first-order inviscid unsteady flow.
ϕ	Complex amplitude of first-harmonic unsteady velocity potential.
ϕ_*	Complex amplitude of first-harmonic convected potential.
Ψ	Stream function for inviscid steady background flow.
Ω	Steady flow angle, Fig, 2.1.
ω	Temporal frequency.

<u>Mathematical</u>

$\tilde{D}/Dt$	Convective derivative operator.
$\bar{D}/Dt$	Convective derivative operator based on mean-flow velocity.
$\text{Im}\{\ \}$	Imaginary part of $\{\ \}$.
$\text{Re}\{\ \}$	Real part of $\{\ \}$.
∇	Gradient operator.
$[\ ]$	Change in a flow quantity across a surface of discontinuity, (2.32).
$<\ >$	Time average, (3.10)
$\|\ \|$	Magnitude of a vector.

Subscripts

B	Reference blade surface.
exc, R, ctrl	Excitation, response, control.
N, T, z, η and ξ	Indicates direction: N — normal to inlet freestream direction, T — parallel to inlet freestream direction, z — out from the page, η — cascade "circumferential" direction, and ξ — cascade axial direction.
$-$, $+$	Axial locations at finite distance upstream and downstream from blade row; point of intersection (ξ_-, η_-) of axial line $\xi = \xi_-$ and reference blade stagnation streamline.
$\mp\infty$	Far upstream/downstream freestream value of a steady flow variable, Fig. 2.1; far upstream/downstream value of an unsteady flow variable.

Superscripts

$'$	Quantity associated with rotor.
$-$	Steady background flow quantity; Circumferential average (3.14)
$\sim$	Time-dependent flow variable.
H	Hermitian (conjugate-transpose) of a matrix.
$*$	Complex conjugate, (3.13).

List of Figures

REPORT DOCUMENTATION PAGE

Public reporting burden for this collection of information is estimated to average 1 hour per response, including the time for reviewing instructions, searching existing data sources, gathering and maintaining the data needed, and completing and reviewing the collection of information. Send comments regarding this burden estimate or any other aspect of this collection of information, including suggestions for reducing this burden, to Washington Headquarters Services, Directorate for Information Operations and Reports, 1215 Jefferson Davis Highway, Suite 1204, Arlington, VA 22202-4302, and to the Office of Management and Budget, Paperwork Reduction Project (0704-0188), Washington, DC 20503.

1. AGENCY USE ONLY (Leave blank)	2. REPORT DATE	3. REPORT TYPE AND DATES COVERED
	December 1993	Final Contractor Report

4. TITLE AND SUBTITLE	5. FUNDING NUMBERS
Active Control of Wake/Blade-Row Interaction Noise Through the Use of Blade Surface Actuators	WU–535–03–10 C–NAS3–25425
6. AUTHOR(S) Kenneth A. Kousen and Joseph M. Verdon	

7. PERFORMING ORGANIZATION NAME(S) AND ADDRESS(ES)	8. PERFORMING ORGANIZATION REPORT NUMBER
United Technologies Research Center 411 Silver Lane, M.S. 129–20 East Hartford, Connecticut 06108–1049	E–8227

9. SPONSORING/MONITORING AGENCY NAME(S) AND ADDRESS(ES)	10. SPONSORING/MONITORING AGENCY REPORT NUMBER
National Aeronautics and Space Administration Lewis Research Center Cleveland, Ohio 44135–3191	NASA CR–4556

11. SUPPLEMENTARY NOTES

Project Manager, Laurence Heidelberg, Propulsion Systems Divsion, (216) 433–3859.

12a. DISTRIBUTION/AVAILABILITY STATEMENT	12b. DISTRIBUTION CODE
Unclassified - Unlimited Subject Categories 07 and 71	

13. ABSTRACT (Maximum 200 words)

This report describes a combined analytical/computational approach for controlling of the noise generated by wake/blade-row interaction through the use of anti-sound actuators on the blade surfaces. A representative two-dimensional section of a fan stage, composed of an upstream fan rotor and a downstream fan exit guide vane (FEGV), is examined. An existing model for the wakes generated by the rotor is analyzed to provide realistic magnitudes for the vortical excitations imposed at the inlet to the FEGV. The acoustic response of the FEGV is determined at multiples of the blade passing frequency (BPF) by using the linearized unsteady flow analysis, LINFLO. Acoustic field contours are presented at each multiple of BPF illustrating the generated acoustic response disturbances. Anti-sound is then provided by placing oscillating control surfaces, whose lengths and locations are specified arbitrarily, on the blades. An analysis is then conducted to determine the complex amplitudes required for the control surface motions to best reduce the noise. It is demonstrated that if the number of acoustic response modes to be controlled is equal to the number of available independent control surfaces, complete noise cancellation can be achieved. A weighted least squares minimization procedure for the control equations is given for cases in which the number of acoustic modes exceeds the number of available control surfaces. The effectiveness of the control is measured by the magnitude of a propagating acoustic response vector, which is related to the circumferentially averaged sound pressure level (SPL), and is minimized by a standard least-squares minimization procedure.

14. SUBJECT TERMS		15. NUMBER OF PAGES
Wake/blade-row interaction; Fan exit guide vane; Vortical excitation; Acoustic response; Active control; Surface actuators; Noise cancellation		38
		16. PRICE CODE A03

17. SECURITY CLASSIFICATION OF REPORT	18. SECURITY CLASSIFICATION OF THIS PAGE	19. SECURITY CLASSIFICATION OF ABSTRACT	20. LIMITATION OF ABSTRACT
Unclassified	Unclassified	Unclassified	

NSN 7540-01-280-5500